Editors' Suggestion

Strong-field ionization of water: Nuclear dynamics revealed by varying the pulse duration

A. J. Howard,[1,2] C. Cheng,[3] R. Forbes,[2,4] G. A. McCracken,[1,2] W. H. Mills,[5] V. Makhija,[5] M. Spanner,[6,7] T. Weinacht,[3] and P. H. Bucksbaum[1,2,4,*]

[1]*Department of Applied Physics, Stanford University, Stanford, California 94305, USA*
[2]*Stanford PULSE Institute, SLAC National Accelerator Laboratory, 2575 Sand Hill Road, Menlo Park, California 94025, USA*
[3]*Department of Physics, Stony Brook University, Stony Brook, New York 11794, USA*
[4]*Department of Physics, Stanford University, Stanford, California 94305, USA*
[5]*Department of Chemistry and Physics, University of Mary Washington, Fredericksburg, Virginia 22401, USA*
[6]*National Research Council of Canada, 100 Sussex Drive, Ottawa, Canada K1A 0R6*
[7]*Department of Physics, University of Ottawa, Ottawa, Canada K1N 6N5*

(Received 14 January 2021; accepted 5 April 2021; published 27 April 2021)

Polyatomic molecules in strong laser fields can undergo substantial nuclear motion within tens of femtoseconds. Ion imaging methods based on dissociation or Coulomb explosion therefore have difficulty faithfully recording the geometry dependence of the field ionization that initiates the dissociation process. Here we compare the strong-field double ionization and subsequent dissociation of water (both H_2O and D_2O) in 10-fs and 40-fs 800-nm laser pulses. We find that 10-fs pulses turn off before substantial internuclear motion occurs, whereas rapid internuclear motion can take place during the double ionization process for 40-fs pulses. The short-pulse measurements are consistent with a simple tunnel ionization picture whose predictions help interpret the motion observed in the long-pulse measurements.

DOI: 10.1103/PhysRevA.103.043120

I. INTRODUCTION

The momentum distribution of ionic fragments following rapid stripping of valence electrons is often used to reconstruct the nuclear geometry of molecules immediately before dissociation [1]. This technique was originally developed with a fast beam of molecules passing through a thin foil to strip away the electrons, but subsequent measurements use intense ultrafast lasers to remove the electrons [2]. The critical difference between these two methods is that the stripping fields of a foil are random, and therefore do not depend on the orientation of the molecules, whereas the laser field is polarized and thus laser-driven ionization can depend strongly on the orientation of the molecule with respect to the laser polarization.

In the tunneling theory of strong-field ionization (SFI), molecular orbitals have preferred orientations that maximize ionization probability with respect to a linearly polarized laser field. Ionization or excitation that prefers a particular alignment based on orbital shape is called geometric alignment. Through this mechanism, an isotropically oriented ensemble of molecules can exhibit strongly anisotropic momentum distributions [3–6].

The strong fields required for laser-driven multiple ionization, on the order of V/Å, can also distort the results by inducing ultrafast motion during ionization [7–10]. One manifestation of this is dynamic alignment, in which an anisotropic polarizability leads to a torque in the presence of a strong field [3]. In SFI experiments on isotropically oriented small molecules with small moments of inertia, dynamic alignment by a linearly polarized laser field drives molecules into rotation and/or bond-angle distortion as the molecules reach a favorable alignment with respect to the laser polarization [4,11–13].

For lighter molecules, both geometric and dynamic alignment play a significant role in femtosecond strong-field ionization, and must both be considered to understand the resulting angle-dependent ionization yields [4,11]. An important parameter that helps to disentangle these two effects is the ionizing pulse duration [8,14–16]. When the pulse duration is much shorter than the timescale of dynamic alignment in the molecule, geometric alignment dominates the angle dependence of the ionization yield. Conversely, when the pulse duration is much longer than this, dynamic alignment can obscure the effects of geometric alignment [17].

Previous work has highlighted that ultrafast molecular motion can align the momenta of dissociating fragment ions in multiply ionized water [8,17–21]. Water is a ten-electron molecule with three filled valence highest occupied molecular orbitals (HOMO, HOMO-1, and HOMO-2) closely analogous to the degenerate $n = 2$, $\ell = 1$ electron orbitals of neon: $2p_x$, $2p_y$, and $2p_z$. The redistribution of electron density among two hydrogens and a noncollinear oxygen breaks both the degeneracy and spherical atomic symmetry so that each orbital is distinguishable [see Fig. 1(a)].

The SFI of water has recently been demonstrated to obey a simple tunneling picture [22], where a strong linearly polarized field selectively ionizes electrons whose nodal plane is perpendicular to the laser polarization axis [3,18,23]. This

*Corresponding author: phbuck@stanford.edu

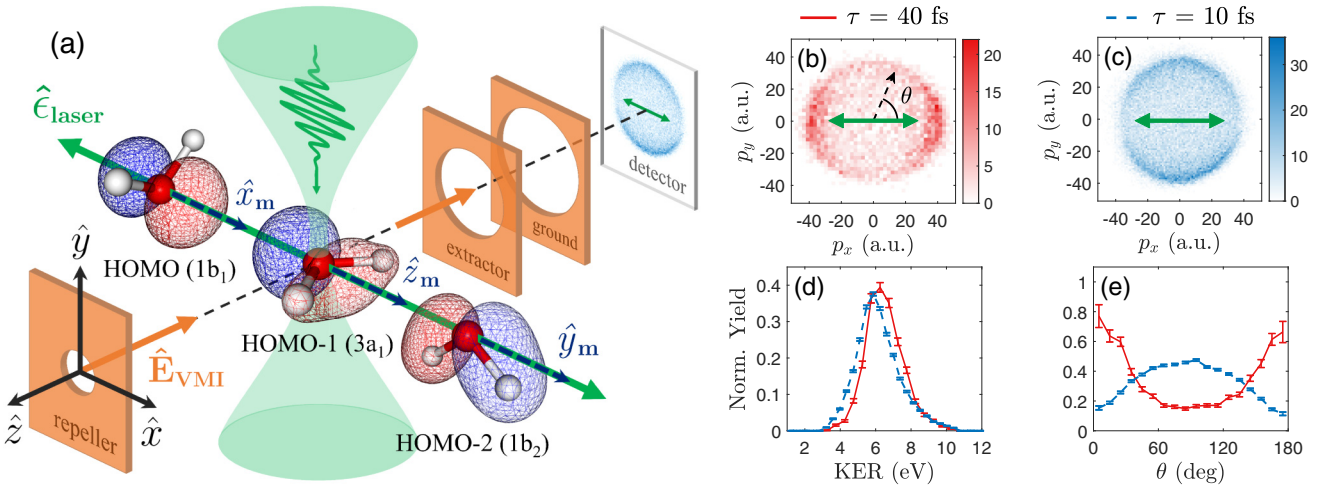

FIG. 1. (a) A schematic rendering of the ionization process and detection geometry. A focused femtosecond laser pulse (green), with polarization $\hat{\epsilon}_{\text{laser}}$ along the $\hat{x}$ direction, removes electrons from the three highest occupied molecular orbitals (HOMO, HOMO-1, and HOMO-2) of neutral water. Preferential ionization of each orbital in a particular orientation with respect to the laser polarization induces geometric alignment as indicated by the molecular axis ($\hat{x}_{\text{m}}/\hat{y}_{\text{m}}/\hat{z}_{\text{m}}$) that is parallel to $\hat{\epsilon}_{\text{laser}}$. After ionization, ionic fragments are accelerated toward the detector screen by an electrostatic lens stack (orange) that applies a constant electric field $\hat{E}_{\text{VMI}}$ in the $\hat{z}$ direction. The net result of this scheme is an image that forms on the detector plane capturing the $\hat{x}$ and $\hat{y}$ momenta of each fragment as well as a distribution of fragment arrival times indicative of the $\hat{z}$ momentum. (b) The $\hat{x}$ and $\hat{y}$ momentum distribution of D^+ ions captured in coincidence with OD^+, following ionization with a 40-fs pulse. The laser polarization axis is drawn as a green arrow. (c) The same distribution as in (b), but following ionization with a 10-fs pulse. (d) The kinetic energy release (KER) distribution plotted for both pulse durations. (e) The angular distribution of D^+ ions where $\theta = \arccos(\hat{\epsilon}_{\text{laser}} \cdot \hat{p}_{D^+})$ represents the angle between the laser polarization axis and the D^+ vector momentum (p_{D^+}), as drawn in panel (b).

leads to simple predictions of the orientation dependence for strong-field ionization, otherwise known as geometric alignment: The HOMO ($1b_1$) orbital should preferentially ionize when the laser polarization is aligned with the $\hat{x}_{\text{m}}$ molecular axis; HOMO-1 ($3a_1$) ionizes for polarization along $\hat{z}_{\text{m}}$, and HOMO-2 ($1b_2$) along $\hat{y}_{\text{m}}$. These three orbitals as well as their preferred alignments with respect to the laser polarization are represented schematically in Fig. 1(a). Such predictions have been supported by both experimental evidence and theoretical strong-field angle-dependent ionization calculations [18,22].

Simple tunneling considerations for each orbital lead to straightforward predictions of the angle-dependent ionization yields for the low-lying states of both the monocation and dication. For example, the doublet ground state of the monocation, D_0 $(1b_1)^{-1}$, should have a maximum ionization yield for laser polarization along $\hat{x}_{\text{m}}$. The triplet ground state of the dication, T_0 $(1b_1)^{-1}(3a_1)^{-1}$, should have a maximum in its ionization yield somewhere within the $\hat{x}_{\text{m}}\hat{z}_{\text{m}}$ plane. These angle-dependent ionization yields are what produce geometric alignment in the monocation and dication populations.

Similar considerations lead to predictions for the dependence of dissociation channels on the occupied molecular orbitals. For example, two-body decays of the dication are expected following the removal of an electron from HOMO or HOMO-1; while three-body decays are expected following the removal of a HOMO-2 electron [24–26]. Significant deviations from such predictions in the tunnel-ionization regime indicate the presence of laser-induced effects such as alignment or internuclear motion in the monocation or the dication [17].

The polarizability of water is very nearly isotropic in its neutral ground state [27], so laser-induced alignment is not expected prior to ionization. However, ultrafast molecular dynamics in the monocation and dication could play a role in dissociation following the second ionization to form H_2O^{2+}. Laser-driven dynamic alignment can also be significant if the ionizing pulse duration significantly exceeds the ∼10 fs needed to realign the H-H axis to the laser polarization before dissociation [17].

Here we compare the dissociation patterns following strong-field ionization of water with laser pulse durations of $\tau = 40$ fs and 10 fs, and with comparable peak intensities of $I_0 = 600$ TW/cm^2 and 400 TW/cm^2, respectively. In each case, all three stable isotopes of water (H_2O, D_2O, and HOD) were doubly ionized and the dissociation of the resultant dication ($H_2O^{2+}/D_2O^{2+}/HOD^{2+}$) was observed using a velocity map imaging (VMI) apparatus, yielding the full three-dimensional (3D) vector momenta of all fragments. For the purposes of data fidelity, the following sections will focus primarily on the experimental results recorded for D_2O^{2+}.

II. EXPERIMENTAL METHODS

The momentum distributions of ions following the double ionization of water with long (40-fs) and short (10-fs) pulses were obtained using two separate VMI systems. Each has been described previously, so only a brief summary is provided here.

The long-pulse experiment employs linearly polarized Ti:sapphire laser pulses with a central wavelength of 800 nm and a pulse duration of $\tau = 40$ fs full width at half maximum (FWHM) [17,18]. The 1-kHz laser is focused to an intensity

of 600 TW/cm^2 at the interaction region of a vacuum chamber (base pressure of 10^{-10} mbar), where it intersects a skimmed effusive molecular beam of the stable isotopes of water (H_2O, D_2O, and HOD). The *in situ* intensity was calibrated by SFI of argon, using a procedure outlined in Ref. [28]. As shown schematically in Fig. 1(a), the interaction region sits at the center of an electrostatic lens stack, allowing the ionic products of SFI to be collected in a VMI spectrometer. The apparatus uses a Roentdek Hexanode detector, with a time resolution of < 1 ns [29], to capture the full 3D vector momenta of the ions produced in the interaction region.

The short pulse experiment uses a 780-nm 30-fs 1-kHz Ti:sapphire system [30,31]. Output pulses from this laser were spectrally broadened in an argon gas filament and recompressed to approximately 10 fs (FWHM) using chirped mirrors and an acousto-optic pulse shaper [32]. The recompressed, linearly polarized pulses are then focused into the interaction region of a vacuum chamber, held at a base pressure of 10^{-10} mbar, by an internally mounted $f = 5$ cm concave spherical mirror. The stable isotopes of water are introduced into the VMI chamber via a skimmed effusive molecular beam. Here, an electrostatic lens stack can be rapidly switched from positive to negative voltages [33] to measure both electrons and ions from each molecule. Directly following ionization, the lens stack accelerates free electrons toward a detector consisting of a microchannel plate (MCP) detector, phosphor screen, and TimePix3 camera [34,35]. Less than 25 ns later, the voltages are reversed and the positive ions are accelerated toward the same detector. With a time resolution of $\sim$1 ns, this detector is able to resolve the 3D vector momenta of all ions, as well as the two-dimensional (2D) vector momenta of the electrons (projected onto the plane of the detector). In this work, only the ion measurements are considered; the electron data were considered in a previous study [22]. Importantly, the rapid voltage switching can introduce slight distortions to the measured momenta of the positive ions. In this experiment, the only substantial distortions were found in the momentum distributions of the lightest fragment, H^+. Due to this effect, we examined both D_2O and H_2O to ensure the validity of our conclusions.

III. RESULTS AND DISCUSSION

A. Two-Body fragment momentum distributions

The relative contributions of geometric and dynamic alignment in the double ionization of water can be observed in the fragment ion momentum distribution of the D_2O^{2+} two-body breakup channel, where D^+ and OD^+ are produced. In this channel, the detector records the full vector momentum for each fragment ion: p_x and p_y are determined by the position of the hit in the detector plane, and p_z is determined by the time of flight (ToF) [see Fig. 1(a)]. The ToF is also used to identify the species of the ion using its unique mass-to-charge ratio [36]. Figures 1(b) and 1(c) are 2D projections along p_z of the momentum distribution in the p_xp_y plane of D^+ ions detected in coincidence with an OD^+ fragment, for long and short pulses, respectively. The angular distributions with respect to the laser polarization axis (drawn as a green arrow) are visibly different. The 40-fs pulse leads primarily to dissociation parallel to the laser polarization axis whereas the 10-fs pulse leads to dissociation perpendicular to the laser polarization. The sum of the kinetic energy of these fragments yields the dissociation kinetic energy release (KER). The KER distributions for D^+/OD^+ is plotted in Fig. 1(d). Note that the long-pulse data are slightly higher in KER, despite the fact that realignment effects would typically reduce the energy of dissociating fragments [37]. This will be discussed further in a later subsection. Calculating the relative angle between the vector momentum of the D^+ ion and the laser polarization yields Fig. 1(e). This plot reaffirms what was noted in comparing Figs. 1(b) and 1(c): the dissociation is parallel to the polarization for long pulses and perpendicular to the polarization for short pulses.

The difference in the dissociation distributions for the short- and long-pulse experiments suggests some evolution on the potential energy surfaces of the monocation or dication before dissociation. If this evolution occurs in the states of the monocation, the double-ionization process must be sequential. The presence of sequential double ionization is supported by an angular correlation analysis of the two electrons produced in coincidence with the dissociating ions, which shows almost no correlation between the electron momenta, in contradiction to results from nonsequential ionization [31,38]. Specifically, the correlation between the $\hat{x}$ component of momentum in the laboratory-frame of each of the two electrons produced in coincidence with D^+/OD^+ was examined. This analysis yielded a correlation coefficient of $r = 0.05$ with a statistical uncertainty of 0.01.

Spectral analysis of the electrons emitted from an isotropic ensemble of neutral D_2O has shown that the first tunnel ionization preferentially populates the doublet ground state of the monocation (D_0) by removing an electron from the b_1 HOMO [22]. The molecular plane is also the nodal plane for the b_1 orbital, so the monocations formed in this way are expected to be preferentially aligned with the molecular plane perpendicular to the laser polarization axis [39] as was confirmed in computations presented in Ref. [22]. The equilibrium geometry of the D_0 state is very near to that of the neutral ground state (X), so the rearrangement of internuclear geometry should be minimal when populating this state [40].

Likewise, the removal of an a_1 electron from the HOMO-1 populates the first excited state of the monocation (D_1), leading to rapid unbending since this state has an equilibrium bend angle, θ_{HOH}, of 180° [40,41]. The distinction between D_0 and D_1, however, is blurred by the presence of the laser. With a central wavelength of 800 nm, the laser is nearly resonant with the D_0 to D_1 transition [40,41]. Strong-field coupling between D_0 and D_1 in this intensity regime should lead to bond-softening distortions in the shape of the D_0 potential, and to rapid unbending [37,42]. The timescale is set by roughly half the period of the unbending mode of the D_1 monocation: $\sim$19 fs for H_2O^+ and HOD^+ and $\sim$26 fs for D_2O^+ [43]. In the short-pulse experiment, the monocation spends only a fraction of 10 fs in the field of the laser before undergoing further ionization followed by rapid dissociation. It is therefore unlikely that the molecule has sufficient time to substantially unbend before dissociation. By contrast, in the long-pulse experiment, full bending dynamics are possible.

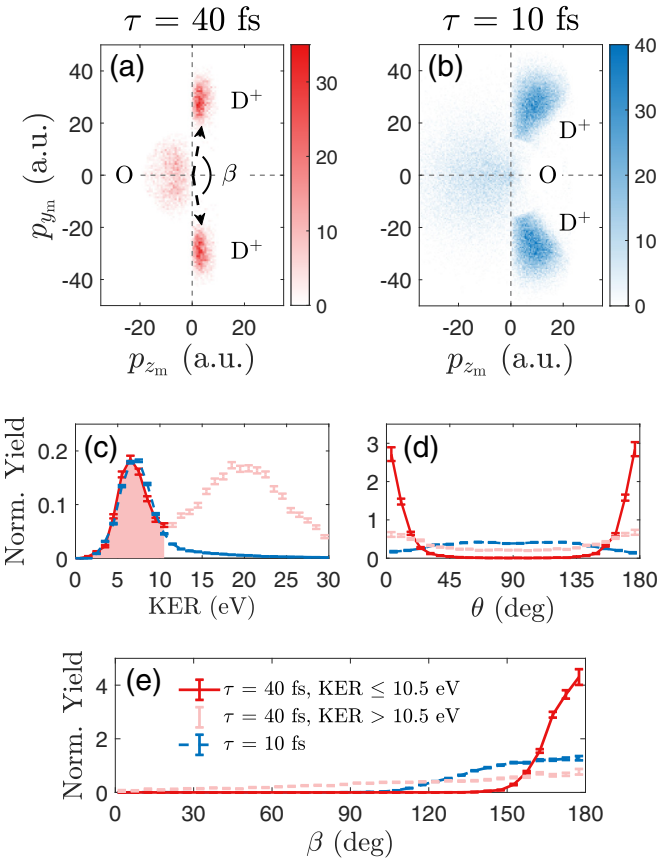

FIG. 2. (a) 2D momentum distributions of the fragments in the three-body breakup channel of the heavy water dication, $D^+/D^+/O$, following ionization by the 40-fs pulse. Here, the bisector between the vector momenta of the two D^+ ions is fixed to be along the horizontal such that the vector momentum of each ion can be decomposed into a component parallel to the bisector p_{z_m} and a component orthogonal to the bisector p_{y_m}. (b) The same as in (a) but following ionization with the 10-fs pulse. (c) The KER distribution for the case of 40 fs (solid red line) and 10 fs (dashed blue line). Light red shading indicates the KER filter used to discriminate between the $D^+/D^+/O$ dication channel (solid red line, shaded) and contamination from the higher-KER $D^+/D^+/O^+$ trication channel (light red markers, unshaded). Here, the 40-fs data were been resized to match the peak height of the 10-fs data. (d) The distribution in angle $\theta = \arccos(\hat{\epsilon}_{\text{laser}} \cdot \hat{y}_m)$, measured between the laser polarization axis ($\hat{\epsilon}_{\text{laser}}$) and the $\hat{y}_m$ molecular axis. (e) The distribution in angle $\beta = \arccos(\hat{p}^{(1)}_{D^+} \cdot \hat{p}^{(2)}_{D^+})$, measured between the two D^+ vector momenta ($p^{(1)}_{D^+}$ and $p^{(2)}_{D^+}$), as drawn in panel (a).

B. Three-Body fragment momentum distributions

The relative lack of unbending motion in the 10-fs data, as compared to the 40-fs data, is best characterized by the three-body fragmentation channel of the D_2O^{2+} dication. In these measurements, the $D^+/D^+/O$ channel is measured via the detection of two D^+ ions in coincidence and the momentum of the undetected neutral oxygen is calculated based on momentum conservation. Defining the molecular frame in momentum space such that the bisector of the two deuterium ions in the plane of the molecule is labeled as p_{z_m} [25,26], our measurements can be viewed as Figs. 2(a) and 2(b) for pulse durations of 40 fs and 10 fs, respectively. Because the third fragment is left undetected, contamination from higher-charge three-body dissociations ($D^+/D^+/O^{n+}$ where n is any positive integer) is possible. As seen in Fig. 2(c), there are two distinct KER signatures in the 40-fs data, whereas in the 10-fs data, there is only one. The higher KER feature in the 40-fs data is indicative of contamination from the $D^+/D^+/O^+$ (trication) dissociation channel where a singly charged oxygen was produced but left undetected. This was verified by directly analyzing the KER distribution in the three-body coincidence $D^+/D^+/O^+$ channel. Because it is distinct in KER, this channel can be effectively filtered out via KER, as seen in Fig. 2(c). This KER-filtered distribution is what is utilized to produce Fig. 2(a). As can be noted in comparing Figs. 2(a) and 2(b), the 10-fs data are spread more diffusely over smaller momentum-frame bend-angles than are the 40-fs data. Figure 2(d) demonstrates that, much like the 40-fs two-body data, the 40-fs three-body data have a strong alignment preference for $\theta = \arccos(\hat{\epsilon}_{\text{laser}} \cdot \hat{y}_m) = 0°$. The alignment preference for the 10-fs three-body data is closer to $\theta = 90°$ and the distribution is substantially less sharp. Figure 2(e) displays the distribution over momentum-frame bend-angle β, reaffirming the disparity in bend-angle found in comparing Figs. 2(a) and 2(b).

It should be noted that although β is closely related to the geometric bend-angle of the molecule upon dissociation θ_{HOH}, the two are distinct from each other. The equilibrium bend angle of neutral water, $(\theta_{\text{HOH}})_{\text{eq.}}$, is 104.5°, whereas in the short-pulse experiment the measured momentum-frame bend angle β ranges from ∼105° to 180°. This disparity can be partially accounted for by some degree of unbending that occurs even in the short-pulse data. This will be explored in depth in a following publication. However, barring any internuclear motion, θ_{HOH} and β would be identical only if the Coulomb repulsion felt by each D^+ ion was exclusively along the direction of its O–D bond. Due to the distribution of charge in the water dication, this is not necessarily the case. For dissociations of higher-charge states in water ($H^+/H^+/O^{n+}$), the momentum-frame bend angle more accurately reflects the geometric bend-angle [8,19].

In addition to launching unbending motion, ionizing with peak intensities in the hundreds of TW/cm^2 can torque the molecule into alignment with the laser polarization if there exists any anisotropy in the molecule's polarizability. Whereas the neutral ground state of water is approximately isotropic in its polarizability, the D_0 and D_1 states of the monocation are not [44]. Recent experimental work has demonstrated that doubly ionizing water with 40-fs pulses at 600 TW/cm^2 induces dynamic alignment such that the $\hat{y}_m$ molecular axis preferentially aligns parallel to the laser polarization prior to dissociation [17]. The characteristic effect of such dynamic alignment in either the three-body $D^+/D^+/O$ or the two-body D^+/OD^+ channel is a peak in dissociation along the laser polarization axis. Looking to Fig. 2(d), such a peak is evident when ionizing with 40-fs pulses. However, this peak is unambiguously missing for the case of a 10-fs pulse. The same is true when considering the two-body dissociation, whereby Fig. 1(e) shows a peak in fragment momenta streaming along the laser polarization axis for the case of 40 fs and not for 10 fs. This suggests there is insufficient time within a 10-fs

pulse for significant alignment to the polarization axis before dissociation.

C. Alignment simulations

Further evidence for the importance of dynamic alignment (particularly its dominance over geometric alignment at longer pulse durations) can be found by turning to simulation. In the laboratory frame, the orientation of a molecule is given by a probability distribution that evolves in time and can be measured relative to a fixed and definite laser polarization axis. We find, however, that the same information can be represented more easily by viewing it in the molecular frame. In this frame, the orientation of the laser polarization axis is no longer fixed, and is instead itself given by a probability distribution that evolves in time and can be measured with respect to fixed and definite molecular axes. This representation is displayed schematically in Fig. 3(a) for the case of a definite laser polarization. Utilizing this same representation, Fig. 3(b) displays the 3D alignment distribution of the monocation directly following the first-ionization event and formation of a 79% D_0 and 21% D_1 mixture of states of D_2O^+. This distribution was calculated via time-dependent resolution in ionic states (TD-RIS), a method of solving the time-dependent Schrödinger equation for a molecule in a strong laser field [45–47]. The method, as applied to water, has been discussed in detail in a previous work [22]. The TD-RIS distribution is computed by solving the electronic ionization dynamics for fixed nuclei and hence includes no nuclear dynamics following the ionization event; it is purely reflective of geometric alignment effects in the water monocation. Here, the laser polarization is predominantly distributed along the $\hat{x}_m$ molecular axis. This result therefore agrees with the intuitive picture of the alignment preference for ionization from the HOMO ($1b_1$), represented schematically in Fig. 1(a).

To explore dynamic alignment effects, these TD-RIS distributions were augmented by rigid-rotor rotational wave packet simulations on the D_0/D_1 mixture of monocations in the presence of a strong field, assuming the geometry of the neutral ground state [48]. The goal is to estimate the dynamic alignment of the monocation immediately prior to dication formation. Since the polarizability anisotropy of D_0 and D_1 are nearly identical, we simulate rotational dynamics using the polarizability tensor of the D_0 state and inertia tensor of the neutral ground state of D_2O [44]. A rotational wave packet is initialized with the molecular axis distribution $P(\theta, \chi)$ consistent with the TD-RIS ionization probability distribution in Fig. 3(a). Here, the Euler angles θ and χ track the alignment of the D-D axis to the laser polarization in the laboratory frame, and the rotation of the oxygen atom around this axis, respectively. To achieve this, the method in Ref. [49] applied to N_2 is adapted to the asymmetric top D_2O, and calculation of the subsequent rotational dynamics proceed as described in prior publications [48,50–52]. The simulation was performed using an initial thermal population at a temperature of 30 K for computational efficiency. Higher temperatures reduce the degree alignment for both the 10-fs and 40-fs pulses, but do not affect the comparison between the two.

Simulating the rotational dynamics in the D_2O^+ monocation for both long and short pulses yield drastically different

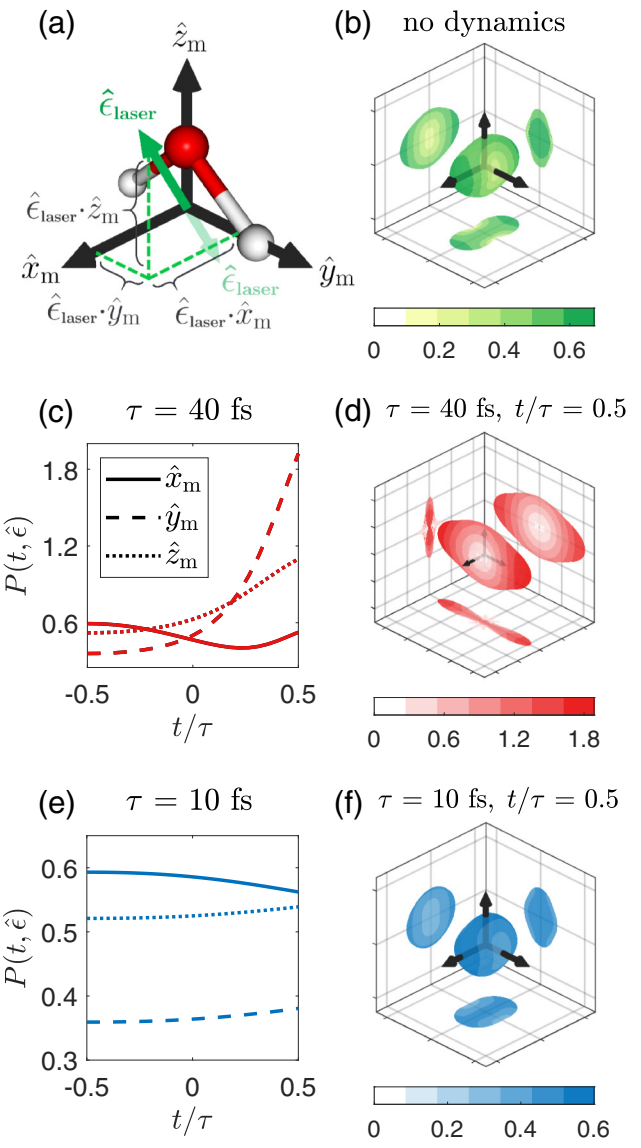

FIG. 3. (a) A schematic drawing of a definite laser polarization ($\hat{\epsilon}_{laser}$) plotted in the molecular frame with each of its projections along the molecular axes ($\hat{x}_m/\hat{y}_m/\hat{z}_m$) labeled. (b) The angle-dependent ionization yield for D_2O^+ (calculated via TD-RIS) represented as a 3D probability distribution of the laser polarization in the molecular frame as seen in (a). (c) The time-resolved alignment distribution of D_2O^+ as characterized by the value of the probability distribution $P(t, \hat{\epsilon})$ along each molecular axis: $\hat{\epsilon} = \hat{x}_m$ (solid line), $\hat{\epsilon} = \hat{y}_m$ (dashed line), and $\hat{\epsilon} = \hat{z}_m$ (dotted line). Here, $P(t, \hat{\epsilon})$ was initiated with the distribution displayed in (b) at $t/\tau = -0.5$ where $t/\tau = 0$ is the time at which the molecule experiences peak field intensity, $I_0 = 600$ TW/cm^2, and $\tau = 40$ fs is the ionizing pulse duration (FWHM). (d) The 3D alignment distribution of D_2O^+ after evolving in a strong field from $t/\tau = -0.5$ to $t/\tau = 0.5$. As in (b), this distribution is represented by the 3D probability distribution of the laser polarization in the molecular frame as seen in (a). Note that the limits of all three axes are double those of (b) to capture the whole distribution. (e) The same as in (c) but for $\tau = 10$ fs and $I_0 = 400$ TW/cm^2. (f) The same as in (d) but for $\tau = 10$ fs and $I_0 = 400$ TW/cm^2. Note that the limits of all three axes are identical to those of panel (b).

results. Figures 3(c) and 3(e) display the time evolution of the monocation's alignment distribution while undergoing laser-driven rotation within a 40-fs and 10-fs pulse, respectively. Both simulations are initiated with the 3D alignment distribution shown in Fig. 3(b) at $t/\tau = -0.5$, where $t/\tau = 0$ corresponds to the peak of the ionizing pulse. Figures 3(d) and 3(f) display the final 3D alignment distribution of the monocation at $t/\tau = 0.5$ for 40-fs and 10-fs pulses, respectively. These distributions are plotted in the same way as Fig. 3(b), displaying the probability distribution of the laser polarization axis in the molecular frame. In comparing the results of 40-fs and 10-fs pulses, we first note in Fig. 3(e) that the orientation of the monocation undergoing alignment within a 10-fs pulse is largely unchanged from the initial orientation. Here the laser polarization is still primarily aligned along $\hat{x}_m$ throughout the duration of the pulse. Because of this lack of significant alignment, the final distribution shown in Fig. 3(f) looks qualitatively similar to the initial distribution shown in Fig. 3(b). By contrast, the orientation of the monocation following alignment within a 40-fs pulse is markedly different. As seen in Fig. 3(c), at early times ($t/\tau < 0$) the degree of alignment along $\hat{x}_m$ decreases gradually while the degree of alignment along $\hat{z}_m$ increases such that briefly around $t/\tau = 0$, the laser polarization is predominantly aligned along the $\hat{z}_m$ axis. Simultaneously, the degree of alignment along $\hat{y}_m$ begins as a small value at early times but increases rapidly over the course of the pulse such that for $t/\tau > 0.2$, the laser polarization becomes overwhelmingly aligned along $\hat{y}_m$. The dramatic enhancement of alignment along $\hat{y}_m$ is made especially clear by viewing the final alignment distribution shown in Fig. 3(d) and comparing to the initial distribution shown in Fig. 3(b).

D. Identifying the contributions of geometric and dynamic alignment

In the short-pulse experiment, we now demonstrate that the angular distribution of fragment ions is largely a consequence of geometric alignment. As a result of our TD-RIS calculations, we estimate that the majority (~79%) of monocations are formed in the $D_0(1b_1)^{-1}$ state. Shown schematically in Fig. 1(a) and numerically in Fig. 3(b), geometric alignment dictates that the removal of an electron from the HOMO will predominantly occur with the laser polarization parallel to the $\hat{x}_m$ molecular axis. A more detailed analysis of the angle-dependent ion yields supports this interpretation [22]. In forming the dication, if the molecule undergoes minimal changes to its internuclear geometry and alignment during the pulse, we should expect the second ionization to occur at the same geometry and alignment as the first. This pathway, $X \rightarrow D_0(1b_1)^{-1} \rightarrow S_0(1b_1)^{-2}$, may therefore be the dominant pathway when producing D^+/OD^+ fragmentation following the sequential double ionization of water using 10-fs pulses.

Further evidence of specifically populating S_0 can be found by looking to electron spectral analysis as well as theoretical modeling of the ions' KER. Electrons captured in coincidence with this two-body decay channel of the water dication have an energy that is characteristic of predominantly ionizing from the HOMO [22]. Separately, according to dissociation simulations of the water dication from the various electronic states [24], the mean value of the KER distribution when dissociating from the S_0 state is approximately 6.15 eV, which agrees very well with the experimental value measured here for the case of $\tau = 10$ fs: 6.17 eV [see Fig. 1(c)].

As for the dissociating ions' angular dependence: we will henceforth consider the two-body dissociation of D_2O^{2+} to occur roughly along the D-D axis (along $\hat{y}_m$). While this is not exactly accurate outside of the limit where $\beta \rightarrow 180^\circ$, this provides an approximate and convenient way to quantify the ions' alignment with respect to the laser polarization. Looking to our 10-fs two-body data, as seen in Fig. 1(c), this interpretation implies that the laser polarization is predominantly orthogonal to $\hat{y}_m$. Therefore, a pathway in which the molecule remains with $\hat{\epsilon}_{laser}$ parallel to $\hat{x}_m$, such as $X \rightarrow D_0(1b_1)^{-1} \rightarrow S_0(1b_1)^{-2}$, is well supported by our experimental observations. However, as seen in Fig. 1(a), all states involving ionization from the HOMO ($1b_1$) or HOMO-1 ($3a_1$) are preferentially formed when either $\hat{\epsilon}_{laser}$ is along the $\hat{x}_m$ or $\hat{z}_m$ direction. Therefore, even those pathways that are preferentially formed at some intermediate orientation between $\hat{x}_m$ and $\hat{z}_m$, such as $X \rightarrow D_0(1b_1)^{-1} \rightarrow T_0(1b_1)^{-1}(3a_1)^{-1}$ would appear in the ion angular distribution as perpendicular to the laser polarization. These pathways may also contribute to this two-body breakup channel.

We now turn to the long-pulse experiment, wherein the effects of dynamic alignment and internuclear motion dominate over geometric alignment. With a pulse duration of 40 fs and peak intensity of 600 TW/cm^2, we expect a significant amount of unbending and re-alignment to occur during the pulse. As seen in Figs. 2(a) and 2(e), the three-body breakup of D_2O^{2+} following long-pulse ionization demonstrates substantial unbending motion, with β ranging from ~145° to 180°. Additionally, both the two-body data [see Fig. 1(e)] and three-body data [see Fig. 2(d)] indicate a large degree of alignment of the $\hat{y}_m$ to the laser polarization, with θ sharply peaked around 0 and 180°.

As indicated by Figs. 3(c) and 3(d), allowing the D_2O^+ monocation to evolve within a $\tau = 40$ fs pulse from $t/\tau = -0.5$ to $t/\tau = 0.5$ results in a significant degree of final alignment along $\hat{y}_m$. However, as we expect the majority of second ionization events to occur around the peak of the pulse ($t/\tau = 0$), the timescale of the full simulation may seem unrealistically long. Here we offer a plausible explanation for more rapid alignment by considering unbending and alignment as coupled actions. In a purely classical picture, one can imagine a small subset of D_2O^+ ions in which one of the two O-D bonds is already initially oriented along the laser polarization axis. A favorable alignment can be reached not only by rotating the molecule around the center of mass, but by rotating a single deuterium about the oxygen by ~75°, simultaneously unbending and aligning the molecule. With rotation and unbending occurring simultaneously, alignment would occur on a faster timescale than what is suggested by Fig. 3(c), as this simulation neglects any and all unbending motion. Additionally, recent simulations of the sequential ionization of water with 20-fs pulses demonstrated that continued unbending motion in the dication is expected prior to dissociation [15]. Therefore coupled unbending and alignment is expected to continue even after the formation of the dication prior to dissociation.

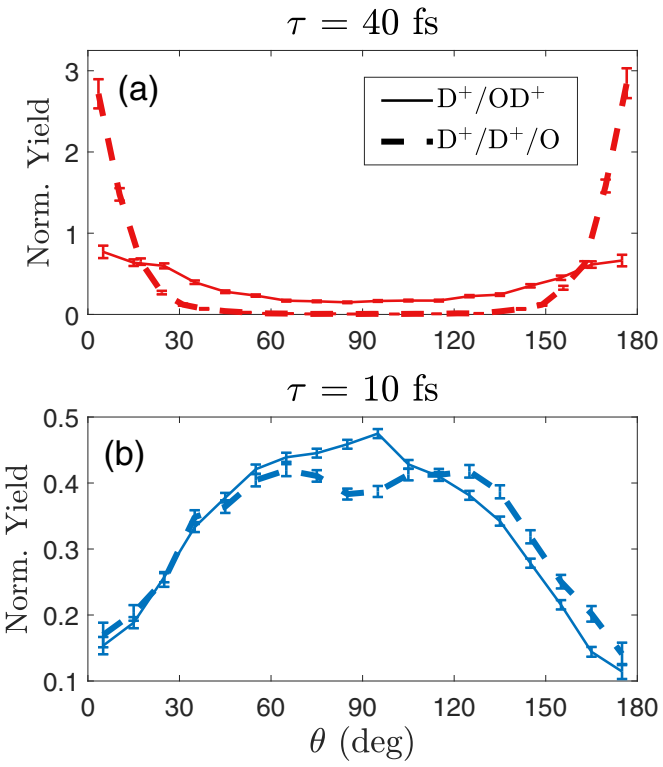

FIG. 4. The angular distribution of both two-body and three-body decay channels, as measured by the angle between the assumed $\hat{y}_m$ molecular axis and the laser polarization ϵ_{laser}. For both (a) the long-pulse data (in red) and (b) the short-pulse data (in blue), the two-body dissociation channel (D^+/OD^+) is plotted as a thin, solid line and the three-body dissociation channel ($D^+/D^+/O$) is plotted as a thick, dashed line. For the two-body channel, θ represents the angle between the dissociation axis and the laser polarization. For the three-body channel $\theta = \arccos(\hat{\epsilon}_{laser} \cdot \hat{y}_m)$.

The two-body and three-body decay channels correlate with different states of the dication: the lower-lying states, such as the $T_0(1b_1)^{-1}(3a_1)^{-1}$ and $S_0(1b_1)^{-2}$, predominantly decay into two bodies, whereas three-body decay occurs predominantly for higher-lying states of the dication, such as the $T_1(1b_2)^{-1}(1b_1)^{-1}$, $T_2(1b_2)^{-1}(3a_1)^{-1}$, and $S_3(1b_2)^{-1}(1b_1)^{-1}$ [24]. Each of these higher-lying states has a vacancy in the HOMO-2 ($1b_2$) orbital. The rules of geometric alignment imply that ionization to these higher-lying states (and subsequent dissociation into three bodies) is enhanced when $\hat{\epsilon}_{laser}$ is along $\hat{y}_m$, so direct comparisons between the two-body and three-body angular distributions should reflect this enhancement. An enhancement along $\theta = 0$ and 180° can be seen in Fig. 4(a) in the three-body channel of the long-pulse experiment compared to the two-body channel. For the same reason, in Fig. 4(b) a more subtle depletion of ion yield at $\theta = 90^\circ$ can been seen in the short-pulse three-body data compared to the two-body data. Thus the long-pulse data, though dominated by dynamic alignment, still bear signatures from geometric alignment.

The simple scenario suggested by Figs. 3(c) and 3(d), wherein long-pulse dynamics in the monocation drive the $\hat{y}_m$ of D_2O^+ into alignment with the laser polarization before ionization to the dication state, still needs some modification because it is not consistent with the predictions of geometric alignment. In this picture, the molecule is aligned with $\hat{y}_m$ parallel to $\hat{\epsilon}_{laser}$ upon formation of the dication. According to geometric alignment, this orientation should correspond to a minimum in ionization yield since the lower-lying states all prefer alignment along either $\hat{x}_m$ or $\hat{z}_m$. However, we observe a clear maximum in ionization yield at this orientation. This inconsistency may be largely alleviated if we assume that unbending and alignment continue to occur in the dication as well as the monocation. In this picture, the dication may be preferentially formed when the molecule is still bent and unaligned (with either $\hat{x}_m$ or $\hat{z}_m$ along the laser polarization), but subsequently unbends and aligns such that $\hat{y}_m$ is largely along $\hat{\epsilon}_{laser}$ during dissociation [15,20]. As we expect the majority of dication formation to occur around $t/\tau = 0$, the predominance of alignment along $\hat{z}_m$ seen in Fig. 3(c) at $-0.2 < t/\tau < 0.2$ supports this picture.

Further evidence for unbending and alignment dynamics in the dication can be found in Fig. 2(c), which shows that the majority of three-body D^+/D^+ coincidences are not from the $D^+/D^+/O$ dication channel, but rather from the $D^+/D^+/O^+$ trication channel with a significantly higher KER signature. This trication contamination is not present in the 10-fs data, suggesting the presence of enhanced multiple ionization in the 40-fs data [18,53]. The dication $D^+/D^+/O$ channel may simply be the remnant dications that were not ionized further during the 40-fs laser pulse. This strong-field enhanced multiple ionization has been observed to be most prevalent for water aligned with the $\hat{y}_m$ molecular axis along the laser polarization [15,17,18].

In fact, the majority of unbending and alignment may occur in the dication and not the monocation. Evidence for this can be seen in Figs. 2(d) and 2(e), comparing the dissociation geometries of the dication (KER $\leqslant$10.5 eV) and trication (KER >10.5 eV) three-body decays in the 40-fs data. Here the dication is more sharply aligned with the field and β is more sharply peaked at 180°, indicating a more linear geometry. As the molecules unbend, many may be ionized to a trication state whereupon they undergo immediate Coulomb explosion while still bent and only partially aligned. Any dications that remain continue to align and unbend before finally dissociating in the three-body channel shown in Fig. 2(a). As seen in Fig. 2(e), the trication signal is spread over a broad distribution of bend-angles, which indicates rapid motion along the bend-angle coordinate in the dication during the formation of the trication.

Our final observation in the comparison of these two data sets is a clear disparity in KER. As seen in Fig. 1(d), the long-pulse two-body KER is noticeably upshifted when compared to the short-pulse two-body KER. This effect is further elucidated by separating out the long-pulse two-body data into two distinct bins: dissociations that occurred parallel to the laser polarization, in which $\theta_\parallel = 0^\circ \pm 30^\circ$ (the majority of counts), and those that occurred perpendicular, in which $\theta_\perp = 90^\circ \pm 30^\circ$. This yields the curves shown in Figs. 5(a) and 5(b) for H_2O and D_2O, respectively. As seen in either panel, the short-pulse KER remains largely unchanged between these two binnings (the two curves lie on top of each other), whereas in the long-pulse experiment the KER measured for parallel dissociations is centered significantly (~1.5 eV) higher than the KER for perpendicular dissociations. This disparity in

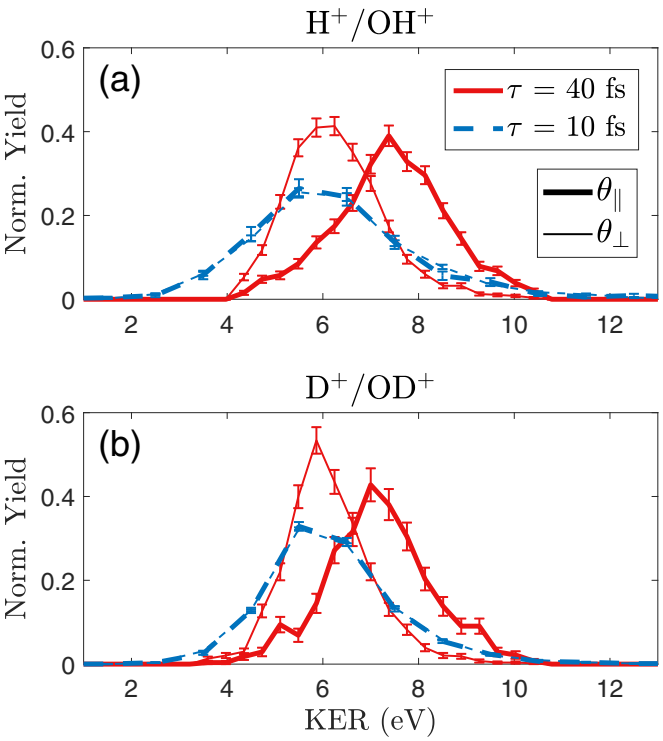

FIG. 5. The KER distribution for the two-body decay pathway of doubly ionized (a) water $H_2O^{2+} \rightarrow H^+/OH^+$ and (b) deuterated water $D_2O^{2+} \rightarrow D^+/OD^+$. In each case, the 40-fs data are plotted in solid red lines, and the 10-fs data are plotted in dashed blue lines. Both long and short-pulse data are further subdivided between dissociation aligned along the laser polarization axis: $\theta_\parallel = 0^\circ \pm 30^\circ$ (thick lines) and dissociation aligned perpendicular to the laser polarization axis: $\theta_\perp = 90^\circ \pm 30^\circ$ (thin lines). All distributions are independently normalized to integrate to 1.

KER between parallel and perpendicular dissociations is not merely due to the preferential formation of different electronic states at different orientations with respect to the laser polarization. If it were, there would exist the same disparity in the short-pulse data. This suggests that coupled rotations, bending, and stretching dynamics, or depletion due to further ionization, all could give rise to this shift in KER, but the precise mechanism is not presently known. Models that predict the KER observed in this experiment may therefore need to include sequential ionization and dissociation with simultaneous unbending and alignment of both the monocation and dication. We know of no work that has attempted such. What we can say definitively is that this phenomenon is reproducible across the varying isotopes of water. As seen by comparing Figs. 5(a) and 5(b), the largest discrepancy between the two isotopes is, predictably, that the D_2O wave packet (on account of its larger mass) is more sharply peaked and more localized in energy-space than is the H_2O wave packet. This observation holds in comparing each of the four curves between the two panels.

IV. CONCLUSION

Close analysis of the two- and three-body fragmentation channels that follow the double ionization of water demonstrate that the physical mechanisms of SFI and fragmentation have a strong dependence on the ionizing pulse duration in the 10-fs to 40-fs range. This has a profound effect on Coulomb-explosion imaging, as expected when applied to molecules with small moments of inertia. We further demonstrated how certain nuclear dynamics in the sequential double-ionization of water can be minimized by ionizing with a sufficiently short pulse duration. In particular, when doubly ionizing water with 40-fs pulses, there appear to be strong distortions to the molecule's internuclear geometry and alignment with respect to the laser polarization axis. This is consistent with the distortions observed in previous work on the water dication [17,18] as well as the higher-charge states of water [8,19]. These effects manifest themselves before dissociation and thus complicate the interpretation of angle-resolved ion yields. However, when ionizing with 10-fs pulses, changes to the molecule's internuclear geometry and alignment are drastically reduced, and angle-resolved ion yields can be interpreted using a greatly simplified model of tunnel ionization. Further detail on the key differences between short- and long-pulse regimes could follow from more comprehensive modeling of these ultrafast processes as well as experiments with more intermediate pulse durations that span the gap between the two pulse durations considered here.

ACKNOWLEDGMENTS

A.J.H., R.F., G.A.M., and P.H.B. were supported by the National Science Foundation. A.J.H. was additionally supported under a Stanford Graduate Fellowship as the 2019 Albion Walter Hewlett Fellow. C.C. and T.W. gratefully acknowledge support from the Department of Energy under Award No. DE-FG02-08ER15984. V.M. and W.H.M. were supported by the Summer Science Institute at University of Mary Washington.

[1] Z. Vager, R. Naaman, and E. P. Kanter, Science **244**, 426 (1989).

[2] H. Stapelfeldt, E. Constant, H. Sakai, and P. B. Corkum, Phys. Rev. A **58**, 426 (1998).

[3] H. Stapelfeldt and T. Seideman, Rev. Mod. Phys. **75**, 543 (2003).

[4] J. H. Posthumus, J. Plumridge, M. K. Thomas, K. Codling, L. J. Frasinski, A. J. Langley, and P. F. Taday, J. Phys. B **31**, L553 (1998).

[5] A. S. Alnaser, C. M. Maharjan, X. M. Tong, B. Ulrich, P. Ranitovic, B. Shan, Z. Chang, C. D. Lin, C. L. Cocke, and I. V. Litvinyuk, Phys. Rev. A **71**, 031403(R) (2005).

[6] D. Pavičić, K. F. Lee, D. M. Rayner, P. B. Corkum, and D. M. Villeneuve, Phys. Rev. Lett. **98**, 243001 (2007).

[7] C. Ellert, H. Stapelfeldt, E. Constant, H. Sakai, J. Wright, D. M. Rayner, and P. B. Corkum, Philos. Trans. R. Soc. London, Ser. A **356**, 329 (1998).

[8] F. Legare, K. F. Lee, I. V. Litvinyuk, P. W. Dooley, S. S. Wesolowski, P. R. Bunker, P. Dombi, F. Krausz, A. D. Bandrauk, D. M. Villeneuve, and P. B. Corkum, Phys. Rev. A **71**, 013415 (2005).

[9] F. Légaré, K. F. Lee, A. D. Bandrauk, D. M. Villeneuve, and P. B. Corkum, J. Phys. B **39**, S503 (2006).

[10] H. Ibrahim, C. Lefebvre, A. D. Bandrauk, A. Staudte, and F. Légaré, J. Phys. B: At. Mol. Opt. Phys. **51**, 042002 (2018).

[11] J. H. Posthumus, J. Plumridge, L. J. Frasinski, K. Codling, A. J. Langley, and P. F. Taday, J. Phys. B **31**, L985 (1998).

[12] K. Miyazaki, T. Shimizu, and D. Normand, J. Phys. B **37**, 753 (2004).

[13] L. B. Madsen, F. Jensen, O. I. Tolstikhin, and T. Morishita, Phys. Rev. A **89**, 033412 (2014).

[14] S. Banerjee, G. R. Kumar, and D. Mathur, Phys. Rev. A **60**, R3369 (1999).

[15] S. Koh, K. Yamazaki, M. Kanno, H. Kono, and K. Yamanouchi, Chem. Phys. Lett. **742**, 137165 (2020).

[16] F. Rosca-Pruna, E. Springate, H. L. Offerhaus, M. Krishnamurthy, N. Farid, C. Nicole, and M. J. J. Vrakking, J. Phys. B **34**, 4919 (2001).

[17] G. A. McCracken and P. H. Bucksbaum, J. Chem. Phys. **152**, 134308 (2020).

[18] G. A. McCracken, A. Kaldun, C. Liekhus-Schmaltz, and P. H. Bucksbaum, J. Chem. Phys. **147**, 124308 (2017).

[19] J. H. Sanderson, A. El-Zein, W. A. Bryan, W. R. Newell, A. J. Langley, and P. F. Taday, Phys. Rev. A **59**, R2567 (1999).

[20] X. M. Tong, Z. X. Zhao, A. S. Alnaser, S. Voss, C. L. Cocke, and C. D. Lin, J. Phys. B: At. Mol. Opt. Phys. **38**, 333 (2005).

[21] S. Zhao, B. Jochim, P. Feizollah, J. Rajput, F. Ziaee, P. Raju P., B. Kaderiya, K. Borne, Y. Malakar, B. Berry, J. Harrington, D. Rolles, A. Rudenko, K. D. Carnes, E. Wells, I. Ben-Itzhak, and T. Severt, Phys. Rev. A **99**, 053412 (2019).

[22] C. Cheng, R. Forbes, A. J. Howard, M. Spanner, P. H. Bucksbaum, and T. Weinacht, Phys. Rev. A **102**, 052813 (2020).

[23] T. K. Kjeldsen, C. Z. Bisgaard, L. B. Madsen, and H. Stapelfeldt, Phys. Rev. A **68**, 063407 (2003).

[24] B. Gervais, E. Giglio, L. Adoui, A. Cassimi, D. Duflot, and M. E. Galassi, J. Chem. Phys. **131**, 024302 (2009).

[25] Z. L. Streeter, F. L. Yip, R. R. Lucchese, B. Gervais, T. N. Rescigno, and C. W. McCurdy, Phys. Rev. A **98**, 053429 (2018).

[26] D. Reedy, J. Williams, B. Gaire, A. Gatton, M. Weller, A. Menssen, T. Bauer, K. Henrichs, P. Burzynski, B. Berry, Z. L. Streeter, J. Sartor, I. Ben-Itzhak, T. Jahnke, R. Dörner, Th. Weber, and A. L. Landers, Phys. Rev. A **98**, 053430 (2018).

[27] D. Spelsberg and W. Meyer, J. Chem. Phys. **101**, 1282 (1994).

[28] W. A. Bryan, S. L. Stebbings, J. McKenna, E. M. L. English, M. Suresh, J. Wood, B. Srigengan, I. C. E. Turcu, J. M. Smith, E. J. Divall, C. J. Hooker, A. J. Langley, J. L. Collier, I. D. Williams, and W. R. Newell, Nat. Phys. **2**, 379 (2006).

[29] O. Jagutzki, A. Cerezo, A. Czasch, R. Dorner, M. Hattas, Min Huang, V. Mergel, U. Spillmann, K. Ullmann-Pfleger, T. Weber, H. Schmidt-Bocking, and G. D. W. Smith, IEEE Trans. Nucl. Sci. **49**, 2477 (2002).

[30] A. Zhao, M. van Beuzekom, B. Bouwens, D. Byelov, I. Chakaberia, C. Cheng, E. Maddox, A. Nomerotski, P. Svihra, J. Visser, V. Vrba, and T. Weinacht, Rev. Sci. Instrum. **88**, 113104 (2017).

[31] C. Cheng, P. Vindel-Zandbergen, S. Matsika, and T. Weinacht, Phys. Rev. A **100**, 053405 (2019).

[32] M. A. Dugan, J. X. Tull, and W. S. Warren, J. Opt. Soc. Am. B **14**, 2348 (1997).

[33] C. S. Lehmann, N. B. Ram, and M. H. M. Janssen, Rev. Sci. Instrum. **83**, 093103 (2012).

[34] M. Fisher-Levine and A. Nomerotski, J. Instrum. **11**, C03016 (2016).

[35] A. Nomerotski, I. Chakaberia, M. Fisher-Levine, Z. Janoska, P. Takacs, and T. Tsang, J. Instrum. **12**, C01017 (2017).

[36] J. Ullrich, R. Moshammer, A. Dorn, R. Dörner, L. P. H. Schmidt, and H. Schmidt-Böcking, Rep. Prog. Phys. **66**, 1463 (2003).

[37] P. H. Bucksbaum, A. Zavriyev, H. G. Muller, and D. W. Schumacher, Phys. Rev. Lett. **64**, 1883 (1990).

[38] W. Becker, X. J. Liu, P. J. Ho, and J. H. Eberly, Rev. Mod. Phys. **84**, 1011 (2012).

[39] J. Muth-Böhm, A. Becker, and F. H. M. Faisal, Phys. Rev. Lett. **85**, 2280 (2000).

[40] J. Leclerc, J. Horsley, and J. Lorquet, Chem. Phys. **4**, 337 (1974).

[41] B. Jayachander Rao and A. J. C. Varandas, Phys. Chem. Chem. Phys. **17**, 6545 (2015).

[42] H. Rottke, C. Trump, and W. Sandner, J. Phys. B: At. Mol. Opt. Phys. **31**, 1083 (1998).

[43] J. E. Reutt, L. S. Wang, Y. T. Lee, and D. A. Shirley, J. Chem. Phys. **85**, 6928 (1986).

[44] R. D. Johnson III, NIST Computational Chemistry Comparison and Benchmark Database, NIST Standard Reference Database Number 101 (2020).

[45] M. Spanner and S. Patchkovskii, Phys. Rev. A **80**, 063411 (2009).

[46] M. Spanner, S. Patchkovskii, C. Zhou, S. Matsika, M. Kotur, and T. C. Weinacht, Phys. Rev. A **86**, 053406 (2012).

[47] M. Spanner and S. Patchkovskii, Chem. Phys. Attos. Spectros., **414**, 10 (2013).

[48] V. Makhija, X. Ren, and V. Kumarappan, Phys. Rev. A **85**, 033425 (2012).

[49] M. Lytova, M. Richter, F. Morales, O. Smirnova, M. Ivanov, and M. Spanner, Phys. Rev. A **102**, 013111 (2020).

[50] T. Seideman and E. Hamilton, in *Advances in Atomic, Molecular, and Optical Physics*, edited by P. R. Berman and C. C. Lin (Academic Press, New York, 2005), Vol. 52, pp. 289–329.

[51] A. Rouzée, S. Guérin, O. Faucher, and B. Lavorel, Phys. Rev. A **77**, 043412 (2008).

[52] S. Pabst, P. J. Ho, and R. Santra, Phys. Rev. A **81**, 043425 (2010).

[53] H. Liu, M. Li, X.-G. Xie, C. Wu, Y.-K. Deng, C.-Y. Wu, Q.-H. Gong, and Y.-Q. Liu, Chin. Phys. Lett. **32**, 63301 (2015).